LASER & PHOTONICS REVIEWS
www.lpr-journal.org

Plasmonic Nanocavity to Boost Single Photon Emission From Defects in Thin Hexagonal Boron Nitride

Mohammadjavad Dowran, Ufuk Kilic, Suvechhya Lamichhane, Adam Erickson, Joshua Barker, Mathias Schubert, Sy-Hwang Liou, Christos Argyropoulos, and Abdelghani Laraoui**

Efficient and compact single photon emission platforms operating at room temperature with ultrafast speed and high brightness will be fundamental components of the emerging quantum communications and computing fields. However, so far, it is very challenging to design practical deterministic single photon emitters based on nanoscale solid-state materials that meet the fast emission rate and strong brightness demands. Here, a solution is provided to this longstanding problem by using metallic nanocavities integrated with hexagonal boron nitride (hBN) flakes with defects acting as nanoscale single photon emitters (SPEs) at room temperature. The presented hybrid nanophotonic structure creates a rapid speedup and large enhancement in single photon emission at room temperature. Hence, the nonclassical light emission performance is substantially improved compared to plain hBN flakes and hBN on gold-layered structures without nanocavity. Extensive theoretical calculations are also performed to accurately model the new hybrid nanophotonic system and prove that the incorporation of plasmonic nanocavity is key to efficient SPE performance. The proposed quantum nanocavity single photon source is expected to be an element of paramount importance to the envisioned room-temperature integrated quantum photonic networks.

1. Introduction

The creation of ultrafast, efficient, and bright single photon emission sources are critical component to realize quantum information systems working with photons as qubits. Deterministic single-photon emitters (SPEs) are observed in a wide range of bulk solid-state systems including color centers in diamonds such as the nitrogen-vacancy (NV)[1–3] and silicon-vacancy (SiV) centers,[4,5] defects and divacancies in silicon carbide,[6–9] and semiconductor quantum dots.[10–12] The unique properties of the host semiconductor materials, mainly their high bandgap (e.g., 5.47 eV for diamond), can host nearby nuclear spins with long coherence times (T_1, T_2) serving as quantum memories/registers.[13,14] These intriguing properties led to the usage of SPEs in many applications including quantum sensing,[15–22] quantum entanglement and teleportation in long distances (>1 km) based on NV diamond spin qubits,[23,24] and quantum memory enhanced quantum communications that operate at megahertz frequencies using SiV centers in diamond.[5] However, these applications suffer from photon nonradiative losses related to the high internal reflections of bulk substrates (e.g., diamond) and refractive index mismatches when integrated into nanophotonic systems.[3,25] Recently, SPEs have been observed in two-dimensional (2D) materials like tungsten diselenide (WSe_2),[26] molybdenum disulfide (MoS_2),[27] and hexagonal boron nitride (hBN).[28–35] Ultrathin 2D hosts facilitate enhanced SPE quantum properties compared to bulk systems due

M. Dowran, A. Erickson, J. Barker, A. Laraoui
Department of Mechanical & Materials Engineering
University of Nebraska-Lincoln
900 N 16th Street, W342 NH, Lincoln, NE 68588, USA
E-mail: alaraoui2@unl.edu

The ORCID identification number(s) for the author(s) of this article can be found under https://doi.org/10.1002/lpor.202400705

DOI: 10.1002/lpor.202400705

U. Kilic, M. Schubert
Department of Electrical and Computer Engineering
University of Nebraska-Lincoln
844 N. 16th Street, Lincoln, NE 68588, USA

S. Lamichhane, S.-H. Liou, A. Laraoui
Department of Physics and Astronomy and the Nebraska Center for Materials and Nanoscience
University of Nebraska-Lincoln
855 N 16th Street, Lincoln, NE 68588, USA

C. Argyropoulos
Department of Electrical Engineering
The Pennsylvania State University
203 Electrical Engineering East, University Park, PA 16802, USA
E-mail: cfa5361@psu.edu

to their narrower emission linewidths in the zero-phonon-line (ZPL),[28–30] the ability to inject carriers by applying large electric fields,[36] improved mechanical properties that allow the realization of mechanical oscillators/cavities with high-quality factor and high resonance frequency,[37] and ease of integration to optical cavities with extremely-small mode volumes for integrated quantum photonics.[25,38,39]

Despite the extensive recent progress in understanding and utilizing the quantum properties of SPEs in 2D systems such as hBN,[28–35] future developments are severely limited by the difficulty of creating SPEs in hBN nanoflakes with desired spectral properties that match the cavity optical frequency modes,[40] and sufficiently high photon emission rates. Numerous methods have been used to increase the fluorescence rates of SPEs in hBN nanoflakes and films. Atomic force microscopy (AFM) was employed to position gold (Au) nanospheres with a diameter of 50 nm in close proximity to SPEs vacancies in hBN flakes and observed an overall fluorescence enhancement of four times with a radiative quantum efficiency of up to 40%.[41] In our previous work, we spread silver nanocubes (SNCs) on top of hBN flakes with a high density (≈0.5 SPE μm^{-2}) of SPEs, and measured a fluorescence enhancement of 200% and slow emission lifetimes in the order of nanoseconds, limited mainly by the spatial and spectral overlap between SPEs and the weak plasmonic field enhancement caused by bare SNCs.[42] Another approach was used recently by spreading SNCs on top of diamond nanocrystals,[43] CdSe/ZnS quantum dots,[12] and WSe_2 flakes[44] deposited on thin metal (Au or Ag) films, hence creating a nanocavity and an overall 300–1900-fold increase in the total fluorescence intensity was obtained. The same metallic nanocavity approach was used very recently to enhance the fluorescence intensity of boron vacancy (V_B^-) emitters in hBN flakes up to 480 times, explained by the large Purcell enhancement.[45,46] These findings are promising for using V_B^- and other quantum emitters in hBN in quantum sensing applications.[47,48] However, the aforementioned results were obtained from ensembles of quantum emitters producing classical light that cannot be used in quantum optical communications where the qubits must be single photons. Recently, optical detected magnetic resonance was observed from SPEs in hBN,[49] urging further enhancement of the SPE quantum properties in hBN for quantum sensing applications.[15,18,50] Hence, the metallic nanocavity enhancement in nonclassical light emission from SPEs in hBN is still missing. The creation of this new type of hybrid plasmonic-hBN single photon source will combine a compact ultrathin design, ultrafast nonclassical light emission rate, high brightness, and room temperature operation. All these properties are ideal for designing a novel deterministic single-photon source platform to be used in envisioned integrated quantum photonic networks and quantum sensing.

Here, we present, for the first time to our knowledge, an architecture for efficient nonclassical light sources by using metallic nanocavities composed of thin hBN flakes (thickness of 35 nm) sandwiched between small plasmonic SNCs (size ≈98 nm) and Au thin film (thickness ≈103 nm) to enhance the quantum properties of SPEs in hBN (**Figure 1**a,b). We demonstrate a substantial enhancement of single photon emission rates at room temperature, manifested by the measured fast emission response in the tens of picoseconds range, due to the designed plasmon nanocavity. Further, we performed rigorous theoretical calculations of excitation enhancement, spontaneous emission enhancement, average electrical field enhancement, and fluorescence enhancement factor of SPEs in SNC/hBN/Au nanocavities. The calculated values fit well with the measured ones taking into account the roughness of the Au films. Our results open the door to the usage of SPEs in compact nanophotonic circuits for quantum optical telecommunications[51] and quantum sensing, [15,18,50] in comparison to other systems such as WSe_2 that work only at cryogenic temperatures.[44]

2. Results and Discussion

2.1. Fabrication of Plasmonic Nanocavity

We first exfoliated hBN flakes from hBN bulk crystals (hq graphene) and transferred them to a SiO_2/Si substrate (Figure S1a, Supporting Information) by using the procedures described in reference.[42] By annealing the hBN/SiO_2/Si substrate in the presence of O_2 (950 sccm) at a temperature of 1100 °C,[42,52] we created a high density (≈0.5 SPE μm^{-2}) of stable emitters, confirmed by confocal fluorescence scanning in Figure S1b (Supporting Information) and anti-bunching $g^{(2)}$ experiments summarized in Table S1 (Supporting Information) (for selected SPEs) Section S4 (Supporting Information). The SPEs may originate from oxygen impurities, substitutional oxygen at N or B sites, and O_2 etching-induced optically active vacancy-related defects.[52–54]

Prior to the transfer of the annealed hBN flakes with SPEs to epitaxial Au films, a Si (111) wafer was cleaned by a sequential sonication process using acetone and isopropyl alcohol to remove any residue. Then, we ion-milled the wafer to remove the top Si layer (≈20 nm thick), to enhance the adhesion during Au deposition. The Au film is sputtered on Si wafer (Figure 1c) at room temperature to achieve a thickness of 103 ± 1 nm, confirmed by AFM in Figure 1d. To perform systematic optical and AFM characterization of the transferred hBN flakes, the Si wafer is marked with a grating of letters. We conducted X-ray diffraction (XRD) analysis of the Au film, revealing a (111) textured Au film (grain size ≈30 nm), as illustrated in Figure S2a (Supporting Information). Following this, we annealed the Au/Si film at 363 °C, resulting in an enhancement of the (111) textured epitaxial characteristics of the Au film, confirmed by a reduction in the XRD linewidth (Figure S2b, Supporting Information), and an increase of the Au grains' size to ≈50–150 nm. Further AFM analysis of the Au grains is described in Section S2 and Figure S3 (Supporting Information).

We followed the procedures described in Section S1 (Supporting Information) to transfer the hBN flakes with a high density of SPEs from SiO_2/Si to Au/Si substrates. It mainly involves using potassium hydroxide (KOH) solution to etch down the SiO_2 layers[55] under hBN to release the flakes with SPEs to be transferred to Au/Si. While this process is reproducible, it resulted in the etching of the hBN flakes and subsequent reduction of the emitter density to ≤0.2 SPE μm^{-2} (discussed in Section 2.2). After measuring the optical quantum properties of the SPEs in the hBN flakes on top of Au/Si, we spin-coated 98 nm SNCs to further enhance the SPE quantum properties due to the plasmonic nanocavity effect. We describe the spin coating process of SNCs on hBN/Au/Si in the Section S5, Supporting Information.

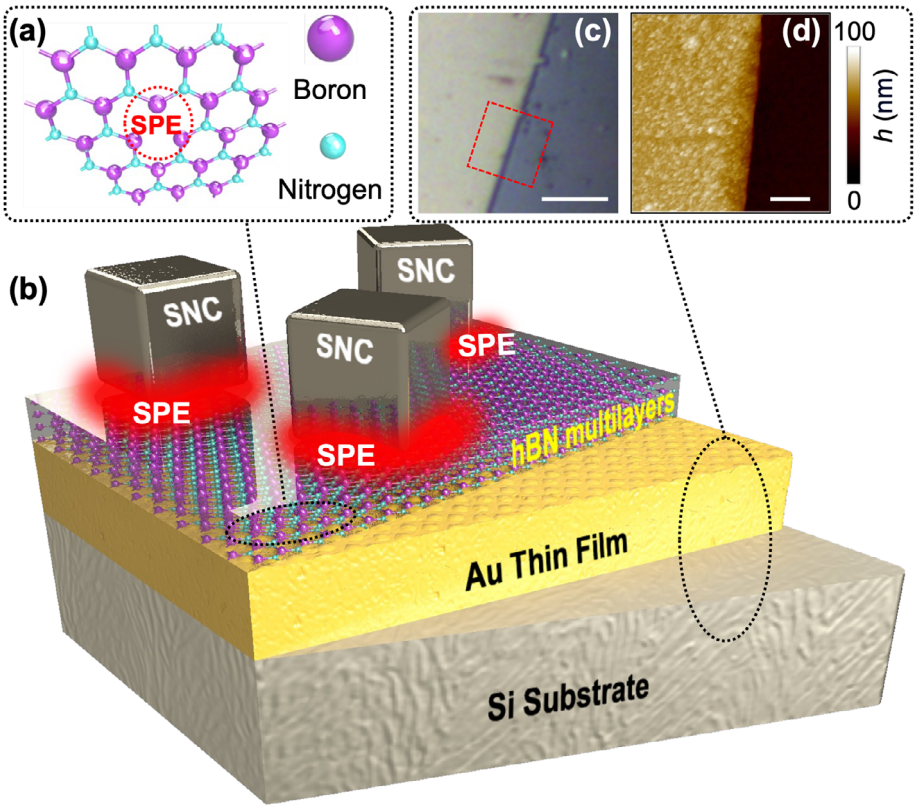

Figure 1. a) Sketch of the hBN flake atoms distribution that exhibits SPE (highlighted with a dashed red circle), composed of nitrogen (purple) and boron (cyan) atoms in a 2D lattice. b) Schematic of hybrid nanophotonic cavity composed of hBN multilayers sandwiched between the Au film and SNCs to enhance the quantum properties of SPEs. c) Optical image of the epitaxial grown Au film on a Si (111) substrate. The scale bar in (c) is 5 µm. d) AFM topography image of the Au/Si substrate highlighted by a dashed square in (c). The scale bar in (d) is 1 µm.

2.2. Optical Characterization of SPEs

To measure at room temperature the quantum properties of SPEs in the hBN flakes transferred to Au/Si substrate with and without SNCs, we used a home-built fluorescence microscope described in reference.[42] We first locate the hBN flakes using a charge-coupled device (CCD) camera as shown in **Figure 2a** and Figure S1c (Supporting Information). The thickness of the flake is 35 ± 5 nm, confirmed by AFM (Figure S1f, Supporting Information). Then, we perform confocal fluorescence imaging of the selected hBN flake to confirm the presence of bright isolated emitters, spectroscopy to check the SPE emission spectrum, $g^{(2)}$ measurements to confirm single photon emission, and finally lifetime measurements.[42] Figures 2b and Fgure S1e (Supporting Information) display the fluorescence maps of a part of the hBN flake, indicated by dashed squares in Figure 2a and Figure S1c (Supporting Information) respectively. Figure 2c shows the normalized fluorescence spectrum of a selected SPE (highlighted in Figure 2b) with full width at half-maximum (FWHM) of 5 ± 0.02 nm at a wavelength of 639.3 nm, attributed to the ZPL of the defect in the hBN flake.[30] The ZPL peaks of 68 studied SPEs occur in the spectral window of 600–760 nm with a negligible phonon side band, corroborating recent studies performed on SPEs in hBN flakes annealed at high temperature of 1100 °C under O_2 flow.[42,52]

To confirm the presence of SPEs in the transferred hBN flakes into the Au/Si substrate, we measured anti-bunching $g^{(2)}$ curves in the Hanbury Brown and Twiss configuration by collecting the SPE fluorescence using two single photon detection modules (PDM, Micro Photon Devices).[42] We found that >50% of the emitters in Figure 2b and Figure S1e (Supporting Information) have a dip of $g^{(2)} < 0.4$ (see Tables S1 and S2, Supporting Information for some of the SPEs without SNCs).[56] The SPEs are highlighted by dashed and solid squares in Figure S1e (Supporting Information) with a density of ≈0.2 SPE µm^{-2}. We normalized and fitted the short-time scale ($t \lesssim 10$ ns) $g^{(2)}$ response of the SPEs (e.g., emitter SPE with the response shown in Figure 2d) to:$g^{(2)}(t) \simeq 1 - (1 + a_1)e^{-t/\tau_1}$, where a_1 is the anti-bunching factor and τ_1 is the decay lifetime which includes both the radiative and nonradiative transition lifetimes.[57,58] We obtain a_1 = -0.84 ± 0.01 and τ_1 = 1.29 ± 0.02 ns by fitting the curve (solid line) in Figure 2d, with $g^{(2)}(0) = 0.15 \pm 0.01$. We further discuss the gold nanograins effects on $g^{(2)}$ in Section 2.3.

2.3. Plasmonic Nanocavity Enhancement of SPE Quantum Properties

We measured the quantum properties at room temperature of SPEs in the hBN flake transferred to Au/Si before (Figure 2a) and after spin-coating of 98 nm ± 7 nm SNCs (Figure S7b, Supporting

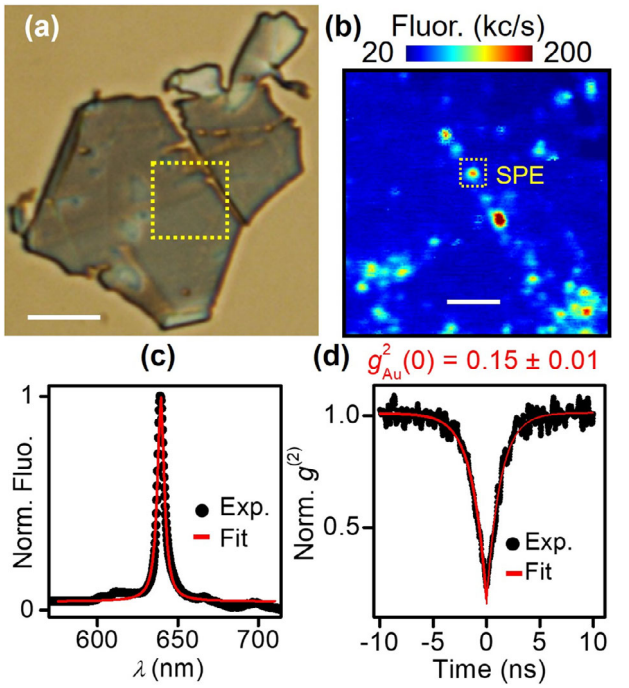

Figure 2. a) Optical image of the studied hBN flake transferred on top of the Au/Si substrate. The scale bar in (a) is 10 µm. b) Confocal fluorescence map of an hBN flake region highlighted by the dashed square in (a), showing the under-study SPE (inside the square). The scale bar in (b) is 2 µm. c) Measured (filled circles) fluorescence intensity spectrum as a function of wavelength of a selected SPE marked in (b). The measured curve is fitted (solid line) with a Lorentzian with an FWHM of 5 ± 0.05 nm. d) Measured (filled circles) autocorrelation $g^{(2)}$ intensity of SPE on Au as a function of the delay time between the two single-photon detection modules. The measured curve is fitted (solid line) with $g^{(2)}(t) \simeq 1 - (1 + a_1)e^{-t/\tau_1}$.

Information). To reduce the high-intensity autofluorescence (up to 5 Mc s^{-1} at saturation) of the SNCs in the spectral window 600–700 nm,[42] we used a set of bandpass (10 nm) filters to isolate SPEs with a narrow emission spectra. However, some of the autofluorescence is still present in the fluorescence maps after spreading SNC with count rates up to 600 kc s^{-1} (see for example Figure S7c, Supporting Information). To further identify the location of selected SPEs (highlighted by squares) after spreading SNCs on top of hBN/Au/Si, we used an overlay method and spectral mapping, respectively.[42] **Figure 3a** shows the fluorescence maps of a selected region of the hBN flake after depositing the SNCs. We can clearly identify most of the SPEs in addition to the SNCs manifested by the small emitting point spread function spots inside and outside the flake (see Figure 3a) due to the local confinement of fluorescence.[59] Upon characterizing the hBN flake transferred on Au/Si in comparison to the flakes located on SiO_2/Si, we see a clear enhancement of the SPEs quantum properties manifested by an increase of the SPEs average saturation fluorescence intensity I_∞ from ≈214 kc s^{-1} to ≈1 Mc s^{-1} (Figure S9a,b, Supporting Information). See for example Figure S1b,e (Supporting Information) measured at a laser power of 1.2 mW. To further assess the effect of Au film and SNCs on the quantum emitters' properties, we measured the second-order photon correlation $g^{(2)}(t)$ of SPEs in the hBN flakes transferred to SiO_2/Si, and Au/Si without and with SNCs.

We focus here on the enhanced quantum properties of selected SPEs in the hBN flakes deposited on SiO_2 (Figure S1b, Supporting Information) and Au/Si (SPE inside the solid square in Figure 3a). We see a narrowing of the emission spectrum of the emitter on Au without and with SNC, as clearly depicted in Figure 3b. We observe a significant narrowing of the $g^{(2)}$ response (Figure 3c) with a decrease of τ_1 from 3.1 ± 0.04 ns in hBN/SiO_2 to 0.51 ± 0.03 ns in hBN/Au/Si without SNC, and to 0.23 ± 0.04 ns in hBN/Au/Si with SNC. While $g^{(2)}(0)$ is 0.013 ± 0.01 for hBN/SiO_2, 0.37 ± 0.01 in hBN/Au/Si without SNC, and 0.48 ± 0.01 in hBN/Au/Si with SNC. The increase in $g^{(2)}(0)$ values for SPEs on hBN/Au/Si substrate with SNC is due to the limited time resolution that is constraint by the decay lifetime of the correlation function of our continuous wave (CW) $g^{(2)}$ setup (≈300 ps).[43] However, all obtained $g^{(2)}(0)$ values are <0.5 which proves that we indeed see single photon emission in all cases (see Tables S1 and S2, Supporting Information). In Tables S1 and S2 (Supporting Information) we confirm that most of the SPEs with excited state lifetime $\tau_1 > 0.3$ ns have indeed $g^{(2)}(0) < 0.4$, confirming the single photon emission.[12,42] In Figure 3d, we plot the histograms of τ_1 values extracted from fitting the measured $g^{(2)}$ curves in 60 SPEs in hBN/SiO_2 and 68 SPEs in hBN/Au/Si, respectively. We extract a mean τ_1 value of 2.85 ± 1.2 ns in hBN/SiO_2 and 0.98 ± 0.33 ns in hBN/Au/Si. The enhancement

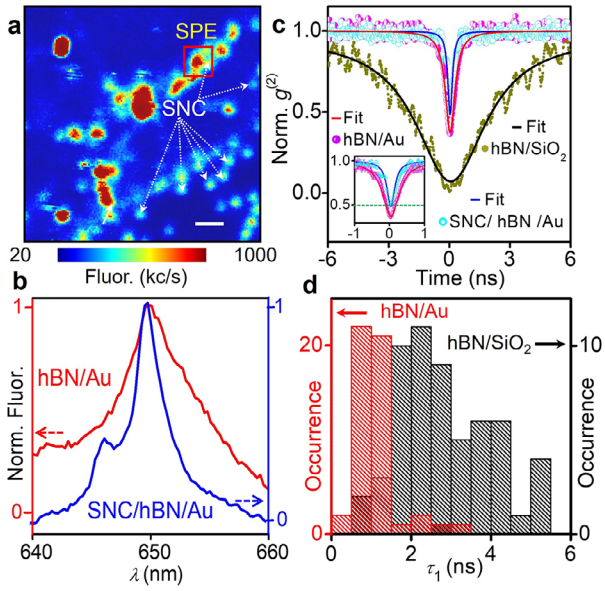

Figure 3. Plasmonic nanocavity enhancement of SPEs quantum properties in SNC/hBN/Au system. a) Fluorescence map of the hBN flake region shown in Figure 2a (indicated by dashed lines) where multiple SNCs are included. The scale bar is 2 µm. The bright emitter SPE (red line box) is coupled with SNC. b) Measured spectrum of the selected SPE before and after depositing the 98-nm SNCs. c) Measured autocorrelation $g^{(2)}$ intensity as a function of time for a selected SPE in hBN flake transferred to SiO_2 (filled circles) and for SPE (highlighted in a) in the hBN flake transferred to Au/Si substrate without (half-filled circles) and with (open circles) SNCs. In the inset of c) we plot the zoomed $g^{(2)}$ for SPE on Au with and without SNC, showing $g^{(2)}(0)$ <0.5. The measured curves are fitted (solid lines). d) Measured τ_1 distribution of 60 SPEs characterized in hBN/SiO_2 (black dashed histogram) and 68 SPEs characterized in hBN/Au (red dashed histograms).

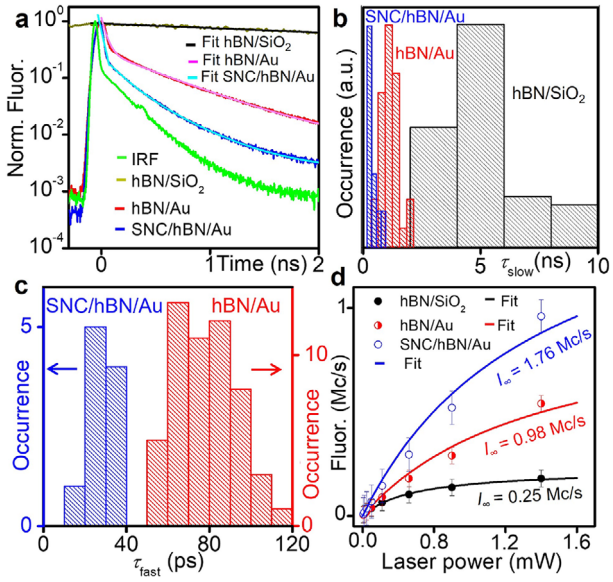

Figure 4. Plasmon nanocavity-assisted enhancement of SPE quantum properties in hBN. a) Measured lifetime response as a function of time for a selected SPE in hBN flake transferred to SiO_2 (solid dark yellow line) and for SPE in the hBN flake transferred to Au/Si substrate without (solid red line) and with (solid blue line) SNCs. The measured curves are fitted (solid lines). The IRF of the setup is plotted as a solid green line. b) Measured τ_{slow} distribution of SPEs characterized in hBN/SiO_2 (gray dashed histogram) and in hBN/Au without (red dashed histograms) and with (blue dashed histogram) SNCs. c) Measured τ_{fast} distribution of SPEs characterized in hBN/Au without (red dashed histograms) and with (blue dashed histogram) SNCs. d) Measured (scattered) and calculated (solid lines) fluorescence intensity as a function of the CW green laser power for a selected SPE in hBN flake transferred to SiO_2 (filled circles) and for SPE (highlighted in Figure 3a) in the hBN flake transferred to Au/Si substrate without (half-filled circles) and with (open circles) SNC.

effect (increase of fluorescence and reduction of τ_1) from just the Au film is explained by the local confinement of electric field at the Au nanograins (see Figure S3d, Supporting Information) due to excited plasmonic hotspots,[60,61] which is confirmed by theoretical modeling (see Section 2.4; Section S7, Supporting Information).

To further distinguish between the enhancement effect from the nanostructured Au film and the metallic nanocavity with SNCs, we measured the excited-state lifetime of 60 SPEs in hBN/SiO_2 and 68 SPEs in hBN/Au with and without SNCs. A 10 ps pulsed 532-nm laser is used to excite the SPEs and we utilize a time-tagger autocorrelation device (PicoHarp 300) to perform time-dependent photon statistics.[42] The time resolution of the lifetime autorotation setup is ≈19 ps, much finer than CW $g^{(2)}$ setup (300 ps), determined from measuring the instrument response function (IRF, green curve in **Figure 4a**) with just green laser pulses (see Section S3, Supporting Information for further details). In Figure 4a, we plot the lifetime curves of SPE in hBN/SiO_2, hBN/Au/Si with and without SNCs. The measured curves of SPEs in hBN/SiO_2 are well-fitted with one exponential decay function $a_3 e^{-t/\tau_{3,\ SiO_2}}$ convoluted with the measured IRF of one of the PDM detectors, where t is time, $\tau_{3,\ SiO_2}$ is the SPE emission lifetime in hBN/SiO_2 that includes both spontaneous and intrinsic nonradiative lifetimes, and a_3 is a weighing factor.[30] The $\tau_{3,\ SiO_2}$ is 5.3 ± 0.6 ns for SPEs in hBN/SiO_2 with a mean value of 5.3 ± 1.16 ns, extracted from the distribution histograms of 60 SPEs (see the gray histogram in Figure 4b). The variation of the excited lifetime of SPEs in hBN/SiO_2/Si substrate is believed to be related to the location of the emitter $d_{z,SPE}$ and/or the nature of the emitter inside the hBN flake.[42]

The measured lifetime curves in hBN/Au without and with SNCs are fitted (solid lines) well with two exponential decay functions convoluted with the measured IRF:[12] $a_{slow}e^{-t/\tau_{slow}} + a_{fast}e^{-t/\tau_{fast}}$, where a_{slow} and a_{fast} are weighing factors. τ_{slow} is the intrinsic lifetime related to the SPEs in hBN and τ_{fast} is the spontaneous emission enhancement lifetime related to the environment that includes both the radiative and nonradiative decays.[62] From the measured lifetime curves in Figure 4a on a selected SPE, τ_{slow} is 0.58 ± 0.02 and 0.29 ± 0.01 ns for hBN/Au without and with SNC respectively. Figure 4b shows the distribution histograms of τ_{slow} from SPEs in hBN/Au without and with SNCs, compared to $\tau_{3,\ SiO_2}$ values obtained from SPEs in hBN/SiO_2. We extract mean τ_{slow} values of 1.15 ± 0.32 ns and 0.88 ± 0.44 ns in hBN/Au without and with SNC simultaneously. However, τ_{fast} = 85 ± 2 ps and 25 ± 1 ps in hBN/Au without and with SNC, respectively. The metallic nanocavity substantially speeds up the spontaneous emission lifetime confirmed by measuring τ_{fast} distribution of 28 SPEs in SNC/hBN/Au nanocavity where enhancement effects are observed with results shown in Figure 4c. We find mean τ_{fast} ($\langle\tau_{fast}\rangle$) values of 85 and 25 ps for SPEs in hBN/Au without and with SNCs, respectively, meaning approximately more than 3.4 times increase in the spontaneous emission rate when SNCs exist.

The plasmon enhancement of SPE's τ_{slow} (the intrinsic lifetime) from the Au film in comparison to the SiO_2 substrate is: $\frac{1/\langle\tau_{slow\ Au}\rangle}{1/\langle\tau_{3,\ SiO_2}\rangle} = \frac{\langle\tau_{3,\ SiO_2}\rangle}{\langle\tau_{slow\ Au}\rangle} = \frac{5.3\ ns}{0.58\ ns} = 9.14$, corresponding to an enhancement factor of ≈9 times, which is a value comparable to the measured enhancement rates in shallow V_{B-} ensemble emitters in hBN flakes deposited on Au striplines.[61] The introduction of nano-grains/rough surface Au thin film leads to increased local density of optical states due to the Purcell effect, which gives rise to both radiative and nonradiative rates[62–64] depending on the distance of SPEs from the Au grains and their respective sizes (50–150 nm). We further detail these effects in the simulation calculations presented in Section 2.4.

We now turn our attention to the effect of SNCs forming a nanocavity on the emission lifetime of the SPEs in hBN/Au. We define the plasmonic nanocavity enhancement of both τ_{slow} and τ_{fast} in hBN/Au with and without SNC as: $\frac{1/\langle\tau_{slow\ Au\ w.\ SNC}\rangle}{1/\langle\tau_{slow\ Au\ w/o\ SNC}\rangle} = \frac{\langle\tau_{slow\ Au\ w/o\ SNC}\rangle}{\langle\tau_{slow\ Au\ w.\ SNC}\rangle} = \frac{0.58\ ns}{0.29\ ns} = 2$, corresponding to an additional enhancement of τ_{slow} of 2 with a total enhancement of τ_{slow} of 18.28. We also see an enhancement of τ_{fast} (spontaneous emission enhancement lifetime): $\frac{1/\langle\tau_{fast\ Au\ w.\ SNC}\rangle}{1/\langle\tau_{fast\ Au\ w/o\ SNC}\rangle} = \frac{\langle\tau_{fast\ Au\ w/o\ SNC}\rangle}{\langle\tau_{fast\ Au\ w.\ SNC}\rangle} = \frac{85\ ps}{25\ ps} = 3.4$. This measured value at the emission wavelength of 650 nm is found to be lower than the FEM simulation prediction of about six times increase which can be spectrally seen in Figure 6c. The difference between these two predictions can be attributed to fabrication imperfections that cannot be taken into account in the simulations and the nonideal dipole alignment of the SPEs that will lead to lower spontaneous emission values in the

theoretical calculations. However, all-in-all the agreement between theory and experiment is very good, as discussed later in the paper. It is also commendable that such a fast response (25 ps) for SPEs in SNCs has not been reported before experimentally in the literature. This overall enhancement of spontaneous emission lifetime is substantially higher than the slow emission response of hBN without the plasmonic structure, since $\frac{1/\langle\tau_{fast\ Au\ w.\ SNC}\rangle}{1/\langle\tau_{3,\ SiO_2}\rangle} = \frac{\langle\tau_{3,\ SiO_2}\rangle}{\langle\tau_{fast\ Au\ w.\ SNC}\rangle} = \frac{5.3\ ns}{25\ ps} = 212$. Such large enhancement can be explained by the metallic plasmonic nanocavity effect,[51] as observed in other SPE systems such as NVs in nanodiamonds[43] and quantum dots.[12,65] However, our hBN-based nanophotonic structure outperforms these previous studies, since quantum dots suffer from fluorescence blinking[66] and nanodiamonds suffer from NV stability and low quantum efficiency (<50%) for smaller nanoscale sizes.[67] In addition, SPEs in hBN have narrow emission lines (<10 nm in comparison to >150 nm for NVs), a highly desirable property for quantum photonics applications.[38] The enhancement factor varies across SPEs in SNC/hBN/Au nanocavity system, as summarized in Table S2 (Supporting Information) (Section S6, Supporting Information) for selected SPEs. For example, the emitter SPE59 (Table S2, Supporting Information) has no enhancement at all and the emitter SPE26 has an enhancement factor of 137.67 times (Figure S12, Supporting Information). This effect is explained by either the non-spatial (e.g., SPE59) or non-spectral (e.g., SPE30) overlap between the SPEs and the plasmonic metallic nanocavity modes in the range of 600–650 and 700–750 nm calculated in Figure S10b. In some of the SPEs (e.g., SPE26), the plasmonic metal nanocavity modes overlap with the spectral emission wavelength of the emitters leading to the narrowing of their ZPL peaks by ≈50% (see inset of Figure S12b, Supporting Information).

However, spontaneous emission enhancement does not mean increased fluorescence, since both radiative and non-radiative rates are enhanced in plasmonic systems.[64] Hence, next, we illustrate the effect of the plasmonic nanocavity on the fluorescence intensity of the SPEs by measuring the saturated count rate I_∞ in hBN/SiO_2, and hBN/Au before and after spreading the SNCs (size of 98 nm). In Figure 4d, we plot the measured (scattered curves) fluorescence intensity of SPE in hBN/SiO_2 and hBN/Au (without and with SNCs) as a function of the CW green laser power. The saturation curves are fitted (solid lines in Figure 4d) to:[41,42] $I = \frac{I_\infty P}{(P_{sat}+P)}$, where P_{Sat} is the saturation power and $I_{\infty,\ SiO2} = 0.25$ Mc/s, $I_{\infty,\ hBN/Au} = 0.98$ Mc/s, and $I_{\infty,\ SNC/hBN/Au} = 1.76$ Mc/s for hBN/SiO_2, hBN/Au, and SNC/hBN/Au substrates, respectively. The overall enhancement factor of the plasmonic nanocavity is $\frac{I_{\infty,\ SNC/hBN/Au}}{I_{\infty,\ SiO2}} = \frac{1.76\ Mc/s}{0.25\ Mc/s} = 7$, corresponding to a fluorescence enhancement of 700%, much higher than the 200% enhancement obtained from just SNC/hBN system reported in reference.[42] We performed similar measurements on 60 SPEs in hBN/SiO_2 and 68 SPEs in hBN/Au with and without SNCs and found a similar mean fluorescence enhancement rate of 7, see Section S6 and Figure S9 (Supporting Information). Our emission enhancement rates are higher than earlier studies reported on SPEs in hBN integrated with metal nanoparticle array (≈2)[68] and nonmetallic (e.g., Si_3N_4) nanocavities (≈6).[69] For example in reference,[68] the measurements were done on just a simple Au plasmonic nanoparticle (NP) array, not nanocavities, i.e., hBN flakes were deposited on Au NPs. The reported fluorescence lifetime enhancement rates in this prior work were ≈270–420 ps, one order of magnitude less than our findings (≈25 ps). Higher fluorescence enhancement rates (> 10) were reported by using bulk cavity modes (volume $\approx\lambda^3$) [70] and fiber-based Fabry–Pérot (FP) cavities.[71] The bulk cavity increases further the single-photon count rate, even at lower excitation powers, due to an enhanced collection efficiency with the cavity,[70] However, the drawback of bulk design is that will be difficult to integrate into photonic circuits. Finally, we also compare the emission enhancement with and without SNC when hBN is on top of the Au substrate: $\frac{I_{\infty,\ SNC/hBN/Au}}{I_{\infty,\ hBN/Au}} = \frac{1.76\ Mc/s}{0.98\ Mc/s} = 1.8$, which is a close to our theoretical calculations of fluorescence enhancement of 2.5 shown in the next section.

2.4. Theoretical Modeling of Plasmonic Systems

To gain a comprehensive understanding of the fast and bright single photon emission performance of the proposed nanophotonic systems, we conducted a series of systematic studies based on 3D simulations using the finite element method. Further details on the simulations created to theoretically investigate the scattering and emission properties, along with additional information on both geometrical and material parameters of the designed single photon emitter are provided in Section S7 (Supporting Information). More specifically, in Figure S10 (Supporting Information), we plot the scattering cross sections of both SPE designs with and without SNCs in the spectral range 500–750 nm as a function of hBN layer thickness in the range of 25–45 nm. Note that the Au substrate is always modeled as a rough surface in both systems to obtain more realistic results. In the case of the absence of SNC, a broad scattering plasmon resonance is obtained which redshifts as a function of hBN layer thickness. On the contrary, when the SNC is present, a narrow resonance is obtained due to the creation of the plasmonic nanocavity, which, interestingly, is also red shifted when the hBN layer thickness is increased.

To understand the measured enhanced quantum properties of the SPE, we illustrate the electric field enhancement factor at the monitoring emission wavelength of 650 nm for SPE designs without and with SNCs, displayed as 2D cross-section slices in **Figure** 5b and Figure 5e, respectively. The incorporation of SNCs leads to a significant enhancement in the electric field induced inside the hBN layer, with the cross-section field enhancement plots demonstrating up to 5 times increase around the edges of the cube at the specified wavelength.

The spatial distribution of the normalized spontaneous emission rate is defined as γ_{sp}/γ_0 (γ_{sp}, γ_0 are the spontaneous emission rates of an emitter placed in the presented nanostructures and the same emitter located at free space, respectively) for the hBN/Au structure design without and with SNC are shown in Figure 5c,f, respectively. The spontaneous emission becomes stronger at the center of the entire space of the hemi-ellipsoidal inclusions which are used to mimic the roughness of Au thin film (more details are provided in Section S7, Supporting Information), leading to the localization of electric field in the proximity of these inclusions. The field gets particularly strong in the location where the

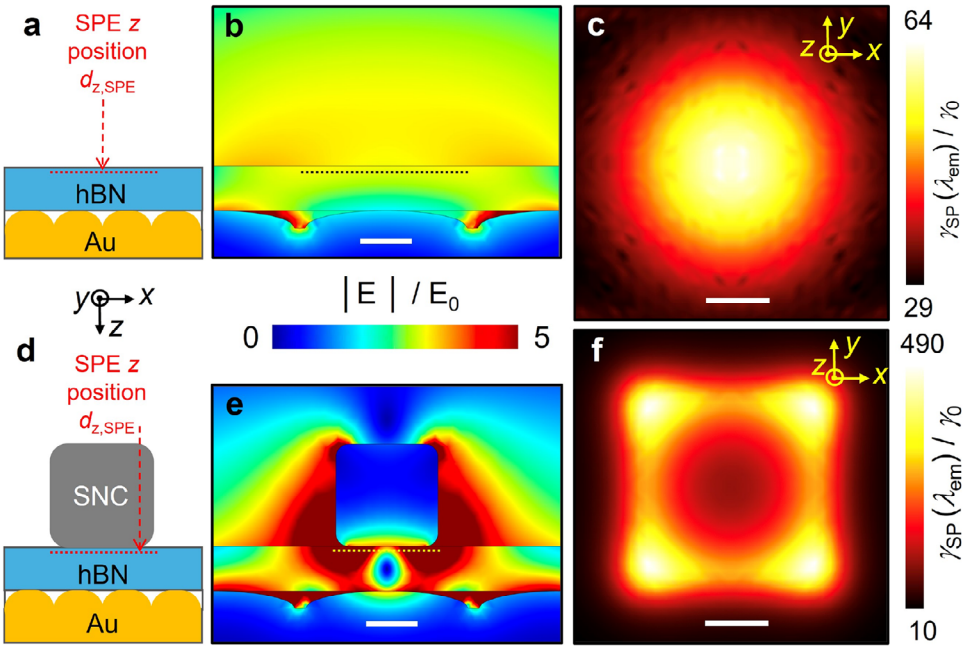

Figure 5. Simulations of the hybrid SNC/hBN/Au nanophotonic systems. Schematic illustration from a central cross-sectional viewpoint of SPE designs a) without and d) with SNC. The electric field enhancement ($|E|/E_0$) is shown along the central cut-slice of each emitter design without b) and with e) SNC at the emission wavelength (λ_{em} = 650 nm). The scale bar in (b) and (e) is 40 nm. The spatial distribution of normalized spontaneous emission rate ($\gamma_{sp}(\lambda_{em} = 650\ nm)/\gamma_0$) is displayed in (c) and (f) for the design without and with SNC, respectively. In these plots, the single photon emitter height ($d_{z\ SPE}$) inside the hBN layer is fixed to 5 nm. The scale bar in (c) and (f) is 20 nm. The emitter height considered in both (c) and (f) is highlighted as a dashed line in the schematic illustrations of the designs (a) without and (d) with SNC.

hemi-ellipsoidal roughness inclusions approach the hBN layer, and it gradually diminishes as one moves up inside hBN (see Figure 5b). For the SPE emitter design with SNC, we observe that the field is stronger beneath the SNC, but it is primarily concentrated near the bottom corners of the SNC (see Figure 5e) despite the Au thin film being rough also in these simulations. Hence, the coupling of the SPE locations in hBN layer to the plasmonic SNC structure acts as an ultra-small mode volume nanocavity.[72,73]

The incorporation of SNC leads to the creation of a plasmonic nanocavity that efficiently couples to SPEs in the hBN layer and, therefore, increases the photonic local density of optical states which leads to the enhancement in the quantum yield.[74] Hence, the formula to compute quantum yield (QY) is $\gamma_r/\gamma_{sp,}$ and here is plotted as a function of wavelength (range of 550–750 nm, **Figure** 6e) and emitter depth (range of 2.5–30 nm, Figure 6f) for the designs with and without SNC. Interestingly, the QY is improved in the case of the nanocavity (with SNC) for the entire wavelength range and emitter depths that we currently investigate. This is in direct agreement with the enhanced fluorescence that was measured in the case of the plasmonic nanocavity.

Note that the experimental lifetime results cannot differentiate between radiative and nonradiative contribution to the photon ultrafast emission but provide the total spontaneous emission as was computed in Figure 5c,f.[63] Interestingly, based on our simulations, we can differentiate which portion of the total spontaneous emission is radiative and nonradiative, respectively. Hence, to further explore the underlying mechanism responsible for the shortened emission lifetime in the case of plasmonic structures, it is essential to compute the radiative decay rate (γ_r) and γ_{sp} in both structure designs without (Figure 6a) and with (Figure 6b) SNC. Note that the computed γ_{sp} is the summation of radiative (γ_r) and nonradiative (γ_{nr}) rates and ideally, we need maximum γ_r and minimum γ_{nr}. In Figure 6c,d, the spectral evolutions of the average normalized spontaneous emission ($\langle\gamma_{sp}(d_{z,SPE})/\gamma_0\rangle$) and radiative decay ($\langle\gamma_r(d_{z,SPE})/\gamma_0\rangle$) rates are presented for both plasmonic emitter designs (without and with SNC), respectively, where their obtained maximum values are averaged along the depth $d_{z,SPE}$ that spans the entire 35 nm thickness of the hBN material. A good agreement is found with measurements of the fast-time emission dynamics, which correspond to spontaneous emission enhancement, as stated before in the experimental result section. The computed γ_r is close to the total spontaneous emission γ_{sp} (that is basically the summation of γ_r and γ_{nr} rates) for both cases without and with SNC at the fixed emission wavelength of 650 nm. Previous studies have already demonstrated that placing the emitter surface close to a metallic thin film leads to quenching and a shortened emission lifetime.[11,63,75–77] Similarly, in the current study, the pronounced roughness of the epitaxial gold thin film leads to some quenching, as can be seen in the lower radiative rate values (Figure 6d) compared to spontaneous emission (Figure 6c), due to the field enhancement (plasmonic hotspots) shown in Figures 5b,e. However, based on our theoretical calculations, the incorporation of the proposed plasmonic nanocavity significantly improves the spontaneous emission performance in the design with SNCs, yielding an average enhancement of approximately

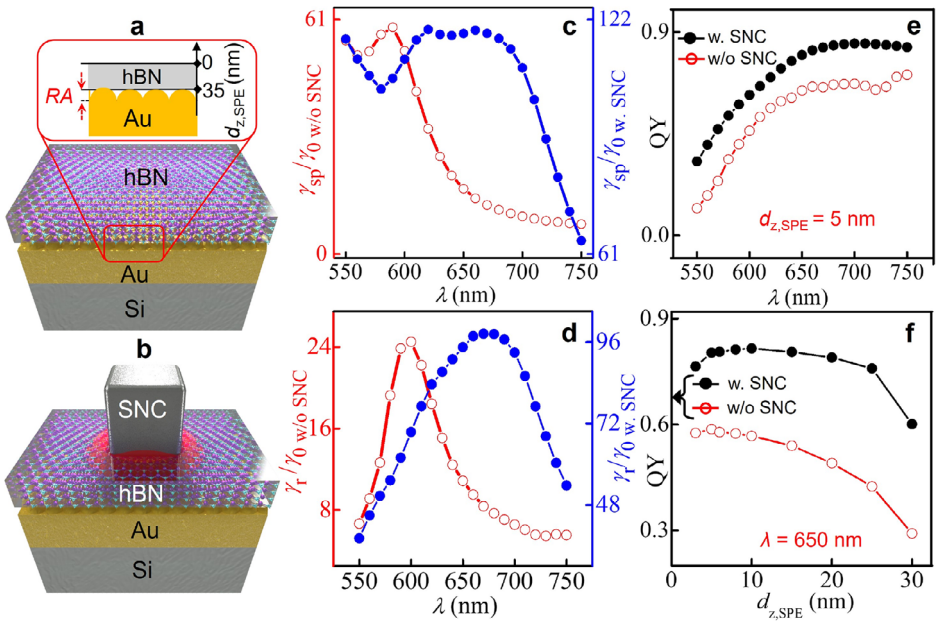

Figure 6. Spectral and depth theoretical analysis of emission properties. a,b) SPE emitter designs without and with SNC are schematically illustrated in (a) and (b), respectively. c,d) The spectral evolutions of (c) average normalized spontaneous emission rates ($\langle\gamma_{sp}(d_{z,SPE})/\gamma_0\rangle$) and d) average normalized radiative decay rate ($\langle\gamma_r(d_{z,SPE})/\gamma_0\rangle$) without (open circles) and with (filled circles) SNCs. e) The quantum yield spectrum (QY ($d_{z,SPE}$ = 5 nm)) and (f) its depth profile analysis (QY (λ_{em} = 650 nm)) for the emitter design without (open circles) and with (filled circles) SNC.

six times compared to the design without SNCs at the emission wavelength of 650 nm (see Figure 6c). As discussed in the experimental section, the spontaneous emission rate is inversely proportional to the excited state lifetime, where the experimentally determined lifetime enhancement between these two cases was computed to be 3.4 at the emission wavelength, which is a value close to the theoretically predicted results.

Finally, the fluorescence enhancement can theoretically be computed by both excitation enhancement ($\gamma_{ex}/\gamma_{ex,0}$) and spontaneous emission (γ_{sp}/γ_0) enhancement, where $\gamma_{ex}/\gamma_{ex,0}$ is directly proportional to the average field enhancement ($|E_{ex}/E_{ex,0}|^2$) inside the hBN SPE computed at the excitation wavelength (532 nm) with (E_{ex}) and without ($E_{ex,0}$) the metallic (plasmonic) structures, i.e., computed at free space.[78,79] Hence, we define the fluorescence enhancement factor (EF) to theoretically analyze the SPE emission brightness performance of the presented plasmonic systems, given as follows:[12,78] $EF = \frac{\eta}{\eta_0}\frac{\gamma_{ex}}{\gamma_{ex,0}}\frac{QY}{QY_0}$, where the enhancement in QY is equal to QY/QY_0, and the normalized collection efficiency is η/η_0. The latter one represents the probability that an emitted photon will reach the detector and is taken as 0.84 for our case due to our experimental detection approach which is very similar to the one used in reference.[12] The QY of each structure is presented in Figure 6e,f. The intrinsic quantum yield of the emitter QY_0 is equal to 0.2, as was shown previously for some of the SPEs in hBN.[80] If we substitute all these computed values inside the fluorescence enhancement factor formula and compare the case of without and with SNC, then we get an approximately average value of 2.5 which is very close to the measured fluorescence counts, where we derived that the ratio between the designs with and without SNC is ≈1.8, as depicted in Figure 4d. Hence, the good agreement between the theoretical enhancement factor predictions and experimental fluorescence counts indicates the accuracy of the simulations in predicting the high radiative quantum efficiency of the emitter design with SNC.[63] Additional factors influencing the overall enhancement of SPE quantum properties in plasmonic nanocavities include the non-spatial and spectral overlap between SNCs (as discussed earlier) and the specific thickness of the hBN film (35 nm). Creating SPEs in thinner (<15 nm) flakes is expected to substantially increase the fluorescence enhancement factor to >1000 times, as obtained from SPEs in QDs with a gap of 12 nm.[12]

3. Conclusion

In summary, we used metallic nanocavities that sustain gap plasmonic modes, integrated with thin hBN multilayered flakes, to achieve an enhancement in the quantum properties of SPEs at room temperature. We first demonstrated a plasmonic enhancement of the SPEs optical properties from the rough substrate Au nanograins, mainly due to plasmonic hotspots induced along the Au film. To further enhance the quantum properties of SPEs on selected thin hBN flakes, we spin-coated SNCs on the Au/Si substrate. The obtained experimental results are explained by rigorous theoretical modeling based on full-wave simulations, where the roughness in the substrate is also considered. Interestingly, such fast emission response (25 ps) for SPEs in SNCs combined with bright fluorescence properties has not been reported before experimentally in the literature and can have a plethora of quantum photonic applications. For example, the presented plasmonic nanocavity enhanced nonclassical light emission can be useful to increase the optically detected magnetic resonance contrast of SPEs observed recently at room temperature,[49] making hBN a promising material for quantum sensing[15] and spin-based photonic quantum applications.[3] More broadly speaking, our results open the door to the usage of

hybrid plasmonic/hBN bright single-photon sources in compact nanophotonic circuits for quantum optical networks that can be used in quantum communications and computing.

Supporting Information

Supporting Information is available from the Wiley Online Library or from the author.

Acknowledgements

This material is based upon work supported by the NSF EPSCoR RII Track-1: Emergent Quantum Materials and Technologies (EQUATE) Award OIA-2044049. A.L. acknowledges additional support from NSF EPSCoR Award OIA-2429381. The research was performed in part in the Nebraska Nanoscale Facility: National Nanotechnology Coordinated Infrastructure and the Nebraska Center for Materials and Nanoscience (and/or NERCF), which are supported by NSF ECCS under Award 2025298, and the Nebraska Research Initiative. C.A. acknowledges partial support from NSF DMR Award 2224456. M.S. acknowledges partial support from NSF ECCS Award 2329940 and AFOSR Award FA9550-21-1-0259.

Conflict of Interest

The authors declare no conflict of interest.

Author Contributions

M.D. and U.K. contributed equally to this work and are co-first authors. M.D. synthesized the hBN flakes, performed the optical measurements and analyzed the data. U.K. performed theoretical modeling, AFM, and Ellipsometry measurements. S.L and S.-H.L prepared the SiO_2/Si and Au/Si substrates and made the marks. A.E. assisted M.D. in the AFM measurements. J.B. performed fluorescence polarization dependence of selected SPEs on SiO_2. C.A. and M.S. assisted U.K. in the theoretical calculations. A.L. and C.A. designed the experiments and supervised the project. A.L., C.A., and U.K. wrote the manuscript with contributions of all authors. All authors have given approval to the final version of the manuscript.

Data Availability Statement

The data that support the findings of this study are available from the corresponding author upon reasonable request.

Keywords

hexagonal boron nitride, metal nanocavity, plasmon, Purcell effect, single photon emitters

Received: May 15, 2024
Revised: September 9, 2024
Published online: October 16, 2024

[1] M. W. Doherty, N. B. Manson, P. Delaney, F. Jelezko, J. Wrachtrup, L. C. L. Hollenberg, *Phys. Rep.* **2013**, *528*, 1.
[2] V. Acosta, P. Hemmer, *MRS Bull.* **2013**, *38*, 127.
[3] M. Atatüre, D. Englund, N. Vamivakas, S.-Y. Lee, J. Wrachtrup, *Nat. Rev. Mater.* **2018**, *3*, 38.
[4] A. Sipahigil, R. E. Evans, D. D. Sukachev, M. J. Burek, J. Borregaard, M. K. Bhaskar, C. T. Nguyen, J. L. Pacheco, H. A. Atikian, C. Meuwly, R. M. Camacho, F. Jelezko, E. Bielejec, H. Park, M. Lončar, M. D. Lukin, *Science* **2016**, *354*, 847.
[5] M. K. Bhaskar, R. Riedinger, B. Machielse, D. S. Levonian, C. T. Nguyen, E. N. Knall, H. Park, D. Englund, M. Lončar, D. D. Sukachev, M. D. Lukin, *Nature* **2020**, *580*, 60.
[6] B. Diler, S. J. Whiteley, C. P. Anderson, G. Wolfowicz, M. E. Wesson, E. S. Bielejec, F. J. Heremans, D. D. Awschalom, *npj Quantum Inf.* **2020**, *6*, 11.
[7] D. J. Christle, A. L. Falk, P. Andrich, P. V. Klimov, J. U. Hassan, N. T. Son, E. Janzén, T. Ohshima, D. D. Awschalom, *Nat. Mater.* **2015**, *14*, 160.
[8] J.-F. Wang, Q. Li, F.-F. Yan, H. Liu, G.-P. Guo, W.-P. Zhang, X. Zhou, L.-P. Guo, Z.-H. Lin, J.-M. Cui, X.-Y. Xu, J.-S. Xu, C.-F. Li, G.-C. Guo, *ACS Photonics* **2019**, *6*, 1736.
[9] W. F. Koehl, B. B. Buckley, F. J. Heremans, G. Calusine, D. D. Awschalom, *Nature* **2011**, *479*, 84.
[10] P. Senellart, G. Solomon, A. White, *Nat. Nanotech* **2017**, *12*, 1026.
[11] E. B. Ureña, M. P. Kreuzer, S. Itzhakov, H. Rigneault, R. Quidant, D. Oron, J. Wenger, *Adv. Mater.* **2012**, *24*, 1202783.
[12] T. B. Hoang, G. M. Akselrod, M. H. Mikkelsen, *Nano Lett.* **2016**, *16*, 270.
[13] A. Laraoui, F. Dolde, C. Burk, F. Reinhard, J. Wrachtrup, C. A. Meriles, *Nat. Commun.* **2013**, *4*, 1651.
[14] C. E. Bradley, J. Randall, M. H. Abobeih, R. C. Berrevoets, M. J. Degen, M. A. Bakker, M. Markham, D. J. Twitchen, T. H. Taminiau, *Phys. Rev. X* **2019**, *9*, 031045.
[15] C. L. Degen, F. Reinhard, P. Cappellaro, *Rev. Mod. Phys.* **2017**, *89*, 035002.
[16] A. Laraoui, J. S. Hodges, C. A. Meriles, *Nano Lett.* **2012**, *12*, 3477.
[17] A. Laraoui, H. Aycock-Rizzo, Y. Gao, X. Lu, E. Riedo, C. A. Meriles, *Nat. Commun.* **2015**, *6*, 8954.
[18] A. Laraoui, K. Ambal, *Appl. Phys. Lett.* **2022**, *121*, 060502.
[19] A. Erickson, S. Q. A. Shah, A. Mahmood, I. Fescenko, R. Timalsina, C. Binek, A. Laraoui, *RSC Adv.* **2023**, *13*, 178.
[20] S. Lamichhane, K. A. McElveen, A. Erickson, I. Fescenko, S. Sun, R. Timalsina, Y. Guo, S.-H. Liou, R. Y. Lai, A. Laraoui, *ACS Nano* **2023**, *17*, 8694.
[21] R. Timalsina, H. Wang, B. Giri, A. Erickson, X. Xu, A. Laraoui, *Adv Elect Mater.* **2024**, *10*, 2300648.
[22] S. Lamichhane, R. Timalsina, C. Schultz, I. Fescenko, K. Ambal, S.-H. Liou, R. Y. Lai, A. Laraoui, *Nano Lett.* **2024**, *24*, 873.
[23] B. Hensen, H. Bernien, A. E. Dréau, A. Reiserer, N. Kalb, M. S. Blok, J. Ruitenberg, R. F. L. Vermeulen, R. N. Schouten, C. Abellán, W. Amaya, V. Pruneri, M. W. Mitchell, M. Markham, D. J. Twitchen, D. Elkouss, S. Wehner, T. H. Taminiau, R. Hanson, *Nature* **2015**, *526*, 682.
[24] S. L. N. Hermans, M. Pompili, H. K. C. Beukers, S. Baier, J. Borregaard, R. Hanson, *Nature* **2022**, *605*, 663.
[25] I. Aharonovich, D. Englund, M. Toth, *Nat. Photon* **2016**, *10*, 631.
[26] K. Parto, S. I. Azzam, K. Banerjee, G. Moody, *Nat. Commun.* **2021**, *12*, 3585.
[27] J. Klein, M. Lorke, M. Florian, F. Sigger, L. Sigl, S. Rey, J. Wierzbowski, J. Cerne, K. Müller, E. Mitterreiter, P. Zimmermann, T. Taniguchi, K. Watanabe, U. Wurstbauer, M. Kaniber, M. Knap, R. Schmidt, J. J. Finley, A. W. Holleitner, *Nat. Commun.* **2019**, *10*, 2755.
[28] I. Aharonovich, J.-P. Tetienne, M. Toth, *Nano Lett.* **2022**, *22*, 9227.
[29] T. T. Tran, C. Zachreson, A. M. Berhane, K. Bray, R. G. Sandstrom, L. H. Li, T. Taniguchi, K. Watanabe, I. Aharonovich, M. Toth, *Phys. Rev. Appl.* **2016**, *5*, 034005.
[30] T. T. Tran, K. Bray, M. J. Ford, M. Toth, I. Aharonovich, *Nat. Nanotech* **2016**, *11*, 37.

[31] T. T. Tran, C. Elbadawi, D. Totonjian, C. J. Lobo, G. Grosso, H. Moon, D. R. Englund, M. J. Ford, I. Aharonovich, M. Toth, *ACS Nano* **2016**, *10*, 7331.
[32] Z.-Q. Xu, C. Elbadawi, T. T. Tran, M. Kianinia, X. Li, D. Liu, T. B. Hoffman, M. Nguyen, S. Kim, J. H. Edgar, X. Wu, L. Song, S. Ali, M. Ford, M. Toth, I. Aharonovich, *Nanoscale* **2018**, *10*, 7957.
[33] C. Li, Z.-Q. Xu, N. Mendelson, M. Kianinia, M. Toth, I. Aharonovich, *Nanophotonics* **2019**, *8*, 2049.
[34] T. Gao, M. von Helversen, C. Antón-Solanas, C. Schneider, T. Heindel, *npj 2D Mater. Appl.* **2023**, *7*, 4.
[35] C. Zhang, Z. Shi, T. Wu, X. Xie, *Adv. Opt. Mater.* **2022**, *10*, 2200207.
[36] F. Xia, H. Wang, D. Xiao, M. Dubey, A. Ramasubramaniam, *Nat. Photon* **2014**, *8*, 899.
[37] J. Chan, T. P. M. Alegre, A. H. Safavi-Naeini, J. T. Hill, A. Krause, S. Gröblacher, M. Aspelmeyer, O. Painter, *Nature* **2011**, *478*, 89.
[38] J. D. Caldwell, I. Aharonovich, G. Cassabois, J. H. Edgar, B. Gil, D. N. Basov, *Nat. Rev. Mater.* **2019**, *4*, 552.
[39] M. Toth, I. Aharonovich, *Annu. Rev. Phys. Chem.* **2019**, *70*, 123.
[40] J. A. Preuß, E. Rudi, J. Kern, R. Schmidt, R. Bratschitsch, S. Michaelis de Vasconcellos, *2D Mater.* **2021**, *8*, 035005.
[41] M. Nguyen, S. Kim, T. T. Tran, Z.-Q. Xu, M. Kianinia, M. Toth, I. Aharonovich, *Nanoscale* **2018**, *10*, 2267.
[42] M. Dowran, A. Butler, S. Lamichhane, A. Erickson, U. Kilic, S. Liou, C. Argyropoulos, A. Laraoui, *Adv. Opt. Mater.* **2023**, *11*, 2300392.
[43] S. I. Bogdanov, M. Y. Shalaginov, A. S. Lagutchev, C.-C. Chiang, D. Shah, A. S. Baburin, I. A. Ryzhikov, I. A. Rodionov, A. V. Kildishev, A. Boltasseva, V. M. Shalaev, *Nano Lett.* **2018**, *18*, 4837.
[44] Y. Luo, G. D. Shepard, J. V. Ardelean, D. A. Rhodes, B. Kim, K. Barmak, J. C. Hone, S. Strauf, *Nat. Nanotech* **2018**, *13*, 1137.
[45] N. Mendelson, R. Ritika, M. Kianinia, J. Scott, S. Kim, J. E. Fröch, C. Gazzana, M. Westerhausen, L. Xiao, S. S. Mohajerani, S. Strauf, M. Toth, I. Aharonovich, Z. Xu, *Adv. Mater.* **2022**, *34*, 2106046.
[46] X. Xu, A. B. Solanki, D. Sychev, X. Gao, S. Peana, A. S. Baburin, K. Pagadala, Z. O. Martin, S. N. Chowdhury, Y. P. Chen, T. Taniguchi, K. Watanabe, I. A. Rodionov, A. V. Kildishev, T. Li, P. Upadhyaya, A. Boltasseva, V. M. Shalaev, *Nano Lett.* **2023**, *23*, 25.
[47] A. J. Healey, S. C. Scholten, T. Yang, J. A. Scott, G. J. Abrahams, I. O. Robertson, X. F. Hou, Y. F. Guo, S. Rahman, Y. Lu, M. Kianinia, I. Aharonovich, J.-P. Tetienne, *Nat. Phys.* **2023**, *19*, 87.
[48] M. Huang, J. Zhou, D. Chen, H. Lu, N. J. McLaughlin, S. Li, M. Alghamdi, D. Djugba, J. Shi, H. Wang, C. R. Du, *Nat. Commun.* **2022**, *13*, 5369.
[49] H. L. Stern, Q. Gu, J. Jarman, S. E. Barker, N. Mendelson, D. Chugh, S. Schott, H. H. Tan, H. Sirringhaus, I. Aharonovich, M. Atatüre, *Nat. Commun.* **2022**, *13*, 618.
[50] A. Laraoui, D. Pagliero, C. A. Meriles, *Phys. Rev. B* **2015**, *91*, 205410.
[51] S. I. Bogdanov, A. Boltasseva, V. M. Shalaev, *Science* **2019**, *364*, 532.
[52] Y. Chen, C. Li, S. White, M. Nonahal, Z.-Q. Xu, K. Watanabe, T. Taniguchi, M. Toth, T. T. Tran, I. Aharonovich, *ACS Appl. Mater. Interfaces* **2021**, *13*, 47283.
[53] P. Ares, H. Santos, S. Lazić, C. Gibaja, I. Torres, S. Pinilla, J. Gómez-Herrero, H. P. Meulen, P. García-González, F. Zamora, *Adv. Electron. Mater.* **2021**, *7*, 2001177.
[54] L. Weston, D. Wickramaratne, M. Mackoit, A. Alkauskas, C. G. Van de Walle, *Phys. Rev. B* **2018**, *97*, 214104.
[55] A. Quellmalz, X. Wang, S. Sawallich, B. Uzlu, M. Otto, S. Wagner, Z. Wang, M. Prechtl, O. Hartwig, S. Luo, G. S. Duesberg, M. C. Lemme, K. B. Gylfason, N. Roxhed, G. Stemme, F. Niklaus, *Nat. Commun.* **2021**, *12*, 917.
[56] O. Iff, Q. Buchinger, M. Moczała-Dusanowska, M. Kamp, S. Betzold, M. Davanco, K. Srinivasan, S. Tongay, C. Antón-Solanas, S. Höfling, C. Schneider, *Nano Lett.* **2021**, *21*, 4715.
[57] S. C. Kitson, P. Jonsson, J. G. Rarity, P. R. Tapster, *Phys. Rev. A* **1998**, *58*, 620.
[58] E. Wu, V. Jacques, H. Zeng, P. Grangier, F. Treussart, J.-F. Roch, *Opt. Express* **2006**, *14*, 1296.
[59] R. Hao, Y. Fan, B. Zhang, *J. Am. Chem. Soc.* **2017**, *139*, 12274.
[60] M. Song, B. Wu, G. Chen, Y. Liu, X. Ci, E. Wu, H. Zeng, *J. Phys. Chem. C* **2014**, *118*, 8514.
[61] X. Gao, B. Jiang, A. E. Llacsahuanga Allcca, K. Shen, M. A. Sadi, A. B. Solanki, P. Ju, Z. Xu, P. Upadhyaya, Y. P. Chen, S. A. Bhave, T. Li, *Nano Lett.* **2021**, *21*, 7708.
[62] C. Ciracì, A. Rose, C. Argyropoulos, D. R. Smith, *J. Opt. Soc. Am. B* **2014**, *31*, 2601.
[63] T. B. Hoang, G. M. Akselrod, C. Argyropoulos, J. Huang, D. R. Smith, M. H. Mikkelsen, *Nat. Commun.* **2015**, *6*, 7788.
[64] G. M. Akselrod, C. Argyropoulos, T. B. Hoang, C. Ciracì, C. Fang, J. Huang, D. R. Smith, M. H. Mikkelsen, *Nat. Photon* **2014**, *8*, 835.
[65] S. Masuo, T. Tanaka, S. Machida, A. Itaya, *J. Photochem. Photobiol.* **2012**, *237*, 24.
[66] S. Wang, C. Querner, T. Emmons, M. Drndic, C. H. Crouch, *J. Phys. Chem. B* **2006**, *110*, 23221.
[67] A. Mohtashami, A. F. Koenderink, *New J. Phys.* **2013**, *15*, 043017.
[68] T. T. Tran, D. Wang, Z.-Q. Xu, A. Yang, M. Toth, T. W. Odom, I. Aharonovich, *Nano Lett.* **2017**, *17*, 2634.
[69] J. E. Fröch, S. Kim, N. Mendelson, M. Kianinia, M. Toth, I. Aharonovich, *ACS Nano* **2020**, *14*, 7085.
[70] T. Vogl, R. Lecamwasam, B. C. Buchler, Y. Lu, P. K. Lam, *ACS Photonics* **2019**, *6*, 1955.
[71] S. Häußler, G. Bayer, R. Waltrich, N. Mendelson, C. Li, D. Hunger, I. Aharonovich, A. Kubanek, *Adv. Opt. Mater.* **2021**, *9*, 2002218.
[72] H. Choi, M. Heuck, D. Englund, *Phys. Rev. Lett.* **2017**, *118*, 223605.
[73] S. Huang, T. Ming, Y. Lin, X. Ling, Q. Ruan, T. Palacios, J. Wang, M. Dresselhaus, J. Kong, *Small* **2016**, *12*, 5190.
[74] V. Giannini, A. I. Fernández-Domínguez, S. C. Heck, S. A. Maier, *Chem. Rev.* **2011**, *111*, 3888.
[75] C. T. Yuan, Y. C. Wang, H. W. Cheng, H. S. Wang, M. Y. Kuo, M. H. Shih, J. Tang, *J. Phys. Chem. C* **2013**, *117*, 12762.
[76] E. Dulkeith, M. Ringler, T. A. Klar, J. Feldmann, A. Muñoz Javier, W. J. Parak, *Nano Lett.* **2005**, *5*, 585.
[77] Z. Liu, A. M. Ricks, H. Wang, N. Song, F. Fan, S. Zou, T. Lian, *J. Phys. Chem. Lett.* **2013**, *4*, 2284.
[78] A. Rose, T. B. Hoang, F. McGuire, J. J. Mock, C. Ciracì, D. R. Smith, M. H. Mikkelsen, *Nano Lett.* **2014**, *14*, 4797.
[79] P. Anger, P. Bharadwaj, L. Novotny, *Phys. Rev. Lett.* **2006**, *96*, 113002.
[80] A. W. Schell, M. Svedendahl, R. Quidant, *Adv. Mater.* **2018**, *30*, 1704237.